Central European Journal of Energetic Materials
ISSN 1733-7178; e-ISSN 2353-1843

Cent. Eur. J. Energ. Mater. 2023, *20*(3): 284-301; DOI 10.22211/cejem/172963
Article is available in PDF-format, in colour, at:
https://ipo.lukasiewicz.gov.pl/wydawnictwa/cejem-woluminy/vol-20-nr-3/

Research paper

Preparation and Characterization of Porous Carbon/ RDX Nanocomposite Energetic Materials

Ju Jiang[1)], **Jin-Xiao Su**[1)], **Zhi-Tao Liu**[1, *)], **Ping Du**[1)], **Xin Liao**[1)], **Xiao-An Li**[2)]

[1)] *School of Chemistry and Chemical Engineering, Nanjing University of Science and Technology, Nanjing, 210014, China*

[2)] *Nanjing Momentum Material Technology Co., Ltd., Nanjing, 211200, China*

**E-mail:* liuzhitao331@163.com

Abstract: A novel energetic material was fabricated by filling porous carbon with 1,3,5-trinitro-1,3,5-triazinane (RDX) via the ultrasonic stirring method. Characterization (TEM, BET, XRD, FTIR, *etc.*) was performed to determine the micromorphology, crystal structure, and specific surface area. TEM images indicated that the RDX particles were homogeneously distributed in the channels of the porous carbon, FTIR spectra and the XRD curve of the C/RDX composite exhibited the combined characteristics of porous carbon and RDX. The BET test data also confirmed this situation. The thermal decomposition kinetics and thermodynamics of the C/RDX nanocomposite energetic material were investigated at various heating rates (5, 10, 15, and 20 $K \cdot min^{-1}$). The test results showed that the thermal decomposition temperature and the critical temperature of thermal explosion were lower than for RDX alone by 46.8 and 40.69 °C, respectively. The activation energy of the C/RDX composite was lower than those of raw RDX and a C/RDX physical mixture, indicating that the C/RDX composite exhibited high thermolysis activity.

Keywords: porous carbon, RDX, nanocomposite materials, thermal decomposition

Nomenclature

β Heating rate [K·min^{-1}]
T_p Temperature of exothermic peak [K]
R Ideal gas constant [8.314 J·mol^{-1}·K^{-1}]
E_a Activation energy [kJ·mol^{-1}]
A Preexponential factor [s^{-1}]
R^2 Correlation coefficient
T_{p0} Extrapolated peak temperature when $\beta \rightarrow 0$ [K]
T_b Critical temperature of thermal explosion [K]

1 Introduction

The microscopic size and structure of energetic materials have a great influence on their combustion and explosion performance. Nanocomposite energetic materials refer to energetic materials such as fuels or oxidants that can be composite at the nanoscale through corresponding technical means, and the specific dispersion and composite scale can be adjusted based on the performance of the material components. Nanoscale contact between materials promotes the heat and mass transfer processes of the materials, and greatly improves the energy release rate of the system [1-3]. Carbon nanomaterials have unique morphology and structure, which endow them with excellent electrical conductivity, thermal conductivity, chemical and mechanical properties. It has been shown that there is too much potential in carbon-based materials to impact an extensive range of technologies including catalysis, desensitization and composites [4-8].

Carbon based materials generally include nano-diamonds, fullerenes, carbon nanotubes, graphene and graphite oxide, *etc*. [9-11]. A carbon-based composite energetic material was fabricated by loading energetic materials in carbon nanotubes [12-15], coating energetic particles with nanodiamonds [16-17], designing graphene-crystal sandwich structures [18], and coating explosives with graphene oxide [19-24]. When energetic crystals are confined within carbon nanostructures, they prevent effective collisions between the crystals and improve impact and friction stability, while utilizing the H-bonding and π-π stacking interactions between the active molecules and the carbon walls to improve electrostatic stability [25]. Moreover, the large specific surface area and high thermal conductivity of carbon materials affects the heat transfer in the reaction, which in turn affects the thermal decomposition process. A carbon-based nanocomposite energetic material with novel structure and excellent performance has been applied in practice [26-29].

Compared to a 3D porous carbon structure, 1D carbon nanotubes or 2D graphene layered nanostructures have lower guest molecule loading capabilities [30]. Because of the interconnected gates and large interior spaces, porous carbon can provide a higher loading efficiency to obtain products with better performance [31]. Shin *et al.* [32] filled high-energy explosives into the inverse opal-like porous carbon (IOC), and achieved precise control of sensitivity to external stimuli. Compared with raw RDX and HMX, the impact, friction and electrostatic stability of the composite materials were greatly improved. Furthermore the excellent performance of the porous carbon/oxidizer composite also provided a proof of concept for a novel family of energetic materials based on porous carbon as the main ingredient [31].

The energetic material prepared by a composite of porous carbon and RDX has a good catalytic performance for the thermal decomposition of RDX, and can reduce its sensitivity. This makes this material able to reduce the hazards in complex environments such as transportation and storage, and also improves its explosive performance. It can be applied in fields such as explosives, fireworks, and propellants.

At present, there are few research reports on the filling of energetic materials into porous carbon. Therefore, in order to further explore the application of porous carbon in energetic materials, porous carbon/RDX nanocomposite energetic materials were prepared using an ultrasonic stirring method, and the morphology, structure, and the sensitivity characteristics of this material were studied.

2. Experimental

2.1 Materials

Porous carbon (S = 2588 m^2/g) was provided by the Nanjing Momentum Technology Co. Ltd.; RDX was purchased from Gansu Yinguang Chemical Co. Ltd.; acetone (C_3H_6O, AR) was obtained from Sinopharm Chemical Reagent Co. Ltd. All experimental water was deionized water.

2.2 Preparation of C/RDX nanocomposite energetic materials

RDX (1.0 g) and acetone (20 mL) were mixed and heated at 20 °C to obtain the RDX solution. After dissolving completely, porous carbon (0.2 g) was added to the solution, followed by ultrasonication for 1 h. The resulting solution was then stirred and treated at a constant temperature of 20 °C for 7 days to complete the process. The product was filtered off (0.2 μm PTFE membrane), washed with deionized water, and dried at 80 °C under moderate vacuum to constant mass.

Weighed amounts of porous carbon powder and RDX in a mass ratio of 1:5, were mixed and ground in a mortar to obtain C/RDX physical mixtures.

2.3 Characterization and tests

The microscopic morphologies of the products were observed with a transmission electron microscope (TEM; JEM-2010plus, JEOL Inc.). The phases were characterized with X-ray diffraction (XRD; D8ADVANCE, Bruker) with Cu-K_a radiation, and the molecular structures were characterized with a Fourier transform infrared spectrophotometer (FTIR; Nicolet6700, Thermal Technology Co., Ltd.). The N_2 adsorption-desorption tests and pore structure parameters of the samples were measured by a low-temperature physical adsorption instrument (BET; ASAP3020, Merck). The thermolysis properties of the products were studied by differential scanning calorimetry (DSC; DSC832E, Mettler-Toledo), the samples (about 0.8 mg) were tested in Al_2O_3 crucibles. The analysis was performed under a pure nitrogen flow (40 mL·min^{-1}) at a heating rate of 10 °C min^{-1}, between 100 to 300 °C. The impact and friction sensitivity were analyzed using a Julius Peters apparatus following the MIL-STD-1751A method (Julius Peters, Berlin). Electrostatic stability was analyzed using an Electrostatic Discharge Tester following the MIL-STD-1751A method (ESD-5KV).

3 Results and Discussion

3.1 TEM

The TEM images of carbon (Figure 1(a)), and the C/RDX composite material (Figure 1(b) and 1(c)) are shown in Figure 1, respectively. The TEM image of the porous carbon (Figure 1(a)) shows that it possesses many pores and interconnected channels. In Figures 1(b) and 1(c), it can be seen that the RDX particles are recrystallized in the carbon channels and their diameters are in the range of 5-10 nm. The RDX particles are evenly distributed.

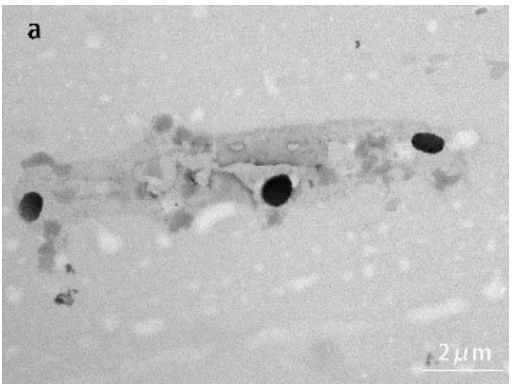

(a)

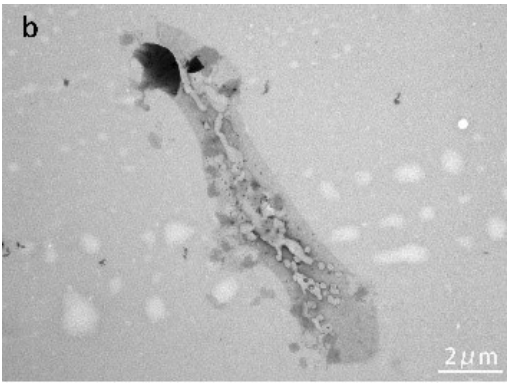

(b)

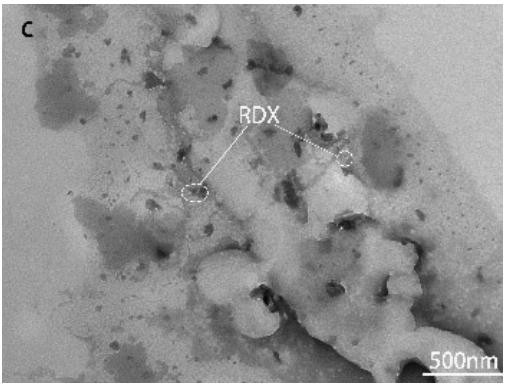

(c)

Figure 1. TEM images of (a) carbon and (b, c) C/RDX composite material

3.2 BET

The N_2 adsorption/desorption data for carbon, and for C/RDX physical mixtures and composites are shown in Figure 2, and exhibit the characteristics of a type I isotherm according to the IUPAC definition, with no obvious hysteresis loop. When the relative pressure is low ($P/P_0 < 0.1$), the adsorption capacity rises sharply with the increase in relative pressure, which indicates the presence of micropores in the sample. Additional confirmation that the RDX is retained in the nanopores of the carbon was provided by gas adsorption, as reflected in the low pore volumes after filling with RDX (these values were lower than for the physical mixtures). The TEM images (Figure 1(c)) of the samples also confirmed this.

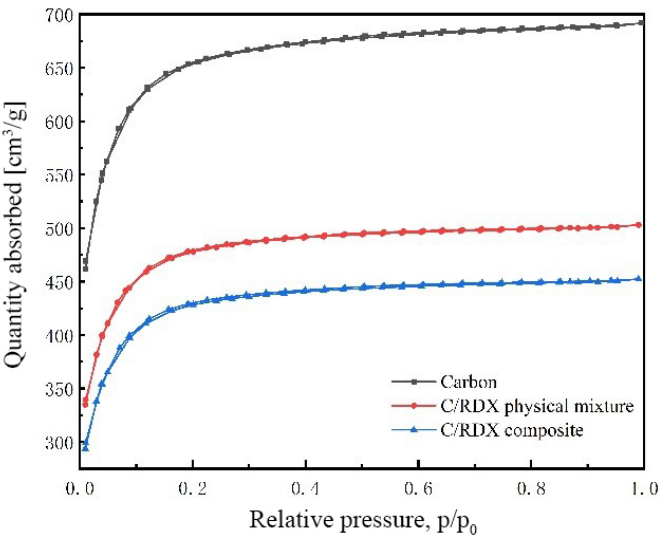

Figure 2. N_2 adsorption-desorption isotherms of carbon, C/RDX physical mixture and C/RDX composite

It can be seen from Figure 3(a) that the pore size distribution of the test material is wide, and that the pore volume increases rapidly with a decrease in the pore size. Within the same interval of pore sizes, the pore volume changes in the range of 0-5 nm which is much larger than that in the range of 5-10 nm. As shown in Figure 3(b), the pore size of all samples showed a multimodal distribution, mainly concentrated below 3 nm. The pore size distribution results indicate that the pore size covers a range from micropore to mesopore, which is consistent with the N_2 adsorption-desorption isotherms.

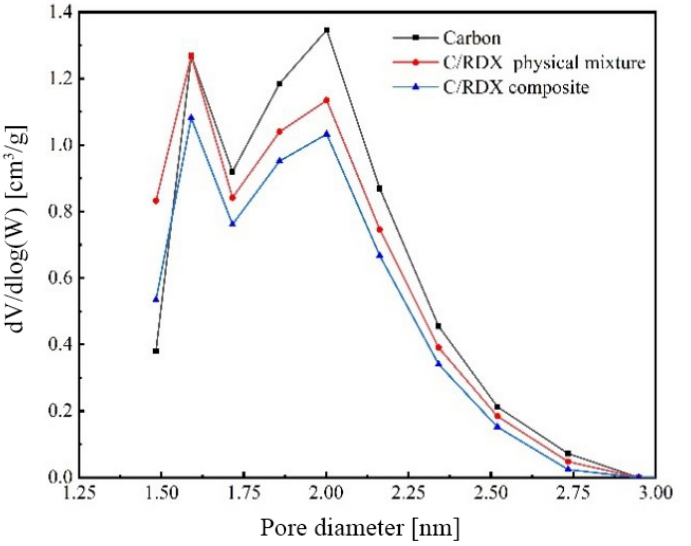

(a)

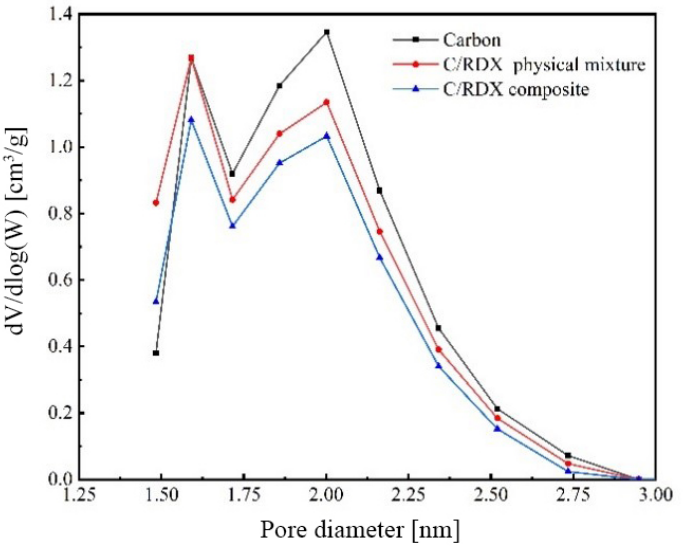

(b)

Figure 3. Pore volume and pore size curve of carbon, C/RDX physical mixture and C/RDX composite (a) and pore size distribution curve of carbon, C/RDX physical mixture and C/RDX composite (b)

In order to observe the changes in pore size distribution more clearly, Table 1 lists the data for the three samples. Compared to pure carbon, the pore size distribution of the C/RDX physical mixture and the C/RDX composite has changed because of the incorporation of RDX, the proportion of micropores has increased, and the proportion of mesopores has decreased. All of the pore structure parameters for these samples are listed in Table 2. It is shown that the pore structure parameters of both the C/RDX physical mixture and the C/RDX composite are significantly lower than the pore structure parameters of porous carbon. The pore structure parameters confirmed that a modification in the fraction of pores in the composite beyond a mass dilution effect of the physical mixtures had occurred.

Table 1. Pore size distribution

Material	Content [%] in the range		
	< 2.0 nm	2.0-2.5 nm	> 2.5 nm
Porous carbon	55.94	39.79	4.25
C/RDX physical mixture	61.39	35.03	3.58
C/RDX composite	60.01	36.80	3.19

Table 2. Pore textural parameters

Material	S_{BET} [m^2/g]	BJH pore volume [cm^3/g]	Average pore diameter [nm]
Porous carbon	2038.18	0.21	2.35
C/RDX physical mixture	1485.27	0.15	2.31
C/RDX composite	1331.63	0.14	2.29

3.3 FTIR

The presence of RDX in C/RDX was also confirmed by FTIR measurements (Figure 4). For the FTIR spectrum of RDX and the C/RDX physical mixture, the peaks at 1532 cm^{-1} are assigned to NO_2 asymmetric stretching. The peaks at 1455 cm^{-1} are related to CH_2 deformation vibrations in the ring of RDX. The bands ranging from 1266 cm^{-1} are ascribed to N–NO_2 stretching vibrations. The peaks at 910 cm^{-1} are ascribed to bending vibrations of the RDX ring and the peaks located at 754 cm^{-1} are assigned to NO_2 stretching. Compared with porous carbon, the partial characteristic peaks for RDX appeared in the C/RDX composite. The peaks at 1340 and 908 cm^{-1} are ascribed to bending vibrations of the RDX ring. It can also be seen that the peaks at 1288 cm^{-1} assigned to NO_2 symmetric stretching, indicated that RDX particles were successfully filled in the porous carbon.

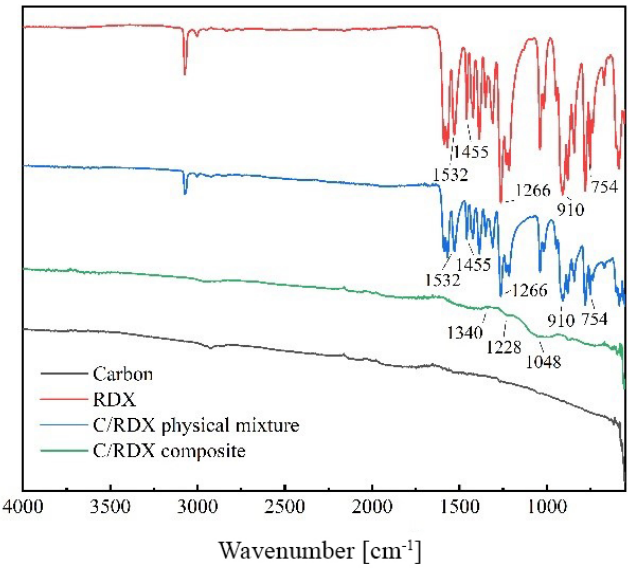

Figure 4. FT-IR spectra

3.4 XRD

Based on the XRD patterns (Figure 5), the crystal form of RDX in the nanocomposite was determined to be α-RDX (No. 44-1619), which is the thermodynamically stable form. After RDX recrystallized inside the carbon, the partial characteristic peaks for RDX which are at 16.58° and 20.386° (2θ) appeared in the C/RDX composite.

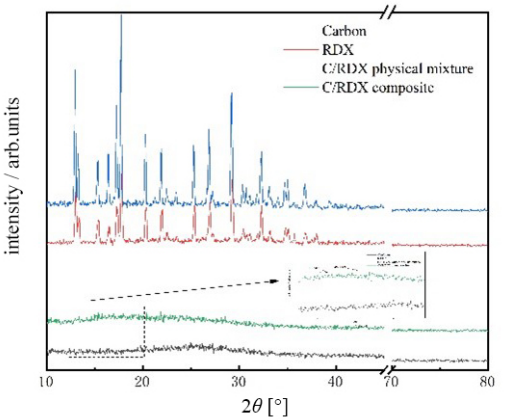

(a)

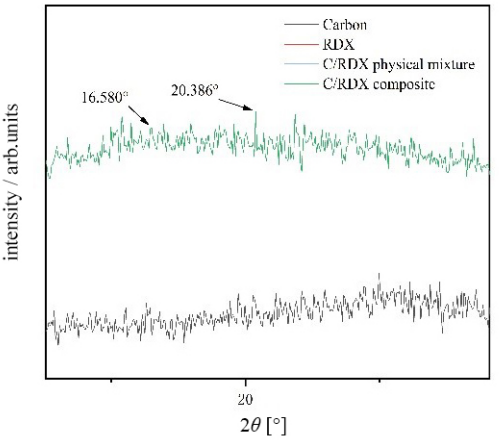

(b)

Figure 5. XRD curves of carbon, RDX, C/RDX physical mixture and C/RDX composite (a) and enlarged detail (b)

3.5 DSC

The thermal decomposition behaviour of RDX, C/RDX physical mixture and C/RDX composite was tested using DSC at a heating rate of 10 K·min^{-1}, as shown in Figure 6. It can be observed that the curve shape of the samples changes: raw RDX shows two exothermic peaks, while the C/RDX physical mixture and the C/RDX composite show one exothermic peak. Compared to that of raw RDX, the endothermic peak temperatures of the C/RDX physical mixture decreased by 7.9 °C, and the endothermic peak was absent for the C/RDX composite. Moreover, the peak decomposition temperatures of the C/RDX physical mixture and the C/RDX composite decreased by 25.9 and 46.8 °C, respectively.

The disappearance of the endothermic peak and the decrease of the exothermic peak temperature are possibly associated with the thermal properties of the nanoparticles [33] or catalysis by the porous carbon [32]. Specifically, it can be attributed to two possible hypotheses. First, porous carbon has an unusually high thermal conductivity. When the system is heated, the heat is quickly conducted to the RDX through the porous carbon, and it is heated rapidly. Then, the processes of melting and decomposition follow. The melting process may be accompanied by a decomposition process, thus the energy released by nano-RDX decomposition may compensate the endothermic process, and thus the endothermic peak disappears. Second, porous carbon has a large number of void defects, which can absorb the strong oxidizing gas generated in the decomposition process of RDX. During the thermal decomposition process,

porous carbon can react with RDX molecular fragments (such as N_2O, NO_2, CH_2O, *etc.*), resulting in weakening of the bond energy of C–N bonds and N–N bonds in RDX molecules and changing the decomposition pathway of the RDX. Compared to the C/RDX physical mixture, the C/RDX composite has a stronger catalytic effect on RDX.

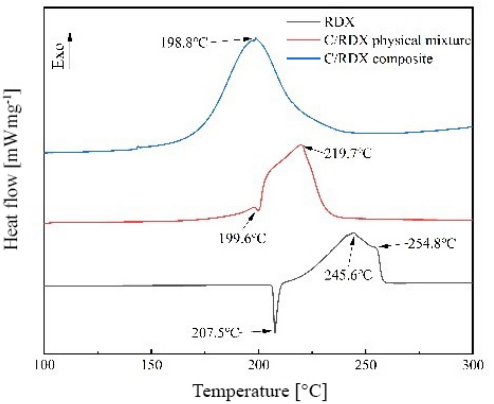

Figure 6. DSC curves of RDX, C/RDX physical mixture and C/RDX composite

In order to further compare the thermal decomposition kinetics of RDX, C/RDX physical mixture and C/RDX composite, DSC tests at heating rates of 5, 10, 15, and 20 $K \cdot min^{-1}$ were performed. The results are shown in Figure 7. From Figure 7(a), it can be seen that as the heating rate increases, the highest decomposition peak temperature of raw RDX is pushed back, and the main peak deformation is sharp. It is obvious from Figure 7(b) that porous carbon has an obvious catalytic effect on the exothermic process of the second stage of RDX. Figure 7(c) shows more clearly that the thermal decomposition of the C/RDX composite is advanced, by almost 40 °C earlier than for raw RDX.

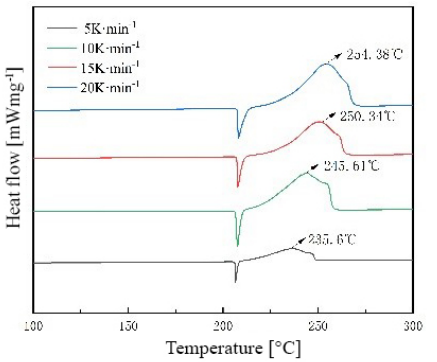

(a)

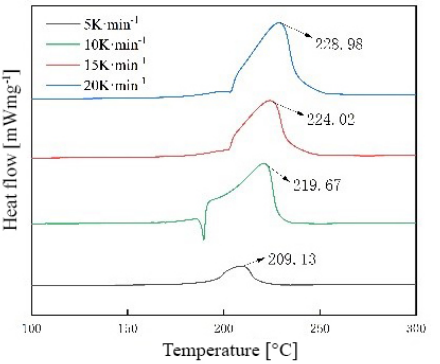

(b)

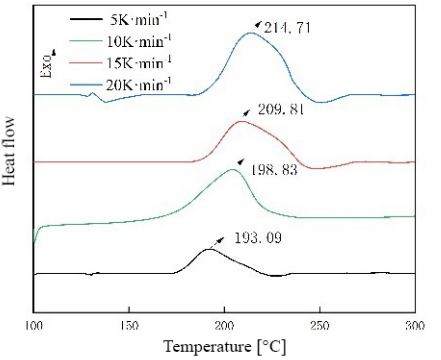

(c)

Figure 7. DSC curves at different heating rates for RDX (a), C/RDX physical mixture (b) and C/RDX composite (c)

The Kissinger and Ozawa equations were used to determine the thermal decomposition kinetic parameters. The T_{p0} and T_b were calculated based on Equations 2 and 3 [34] and the calculated results are listed in Table 3 (E_a in Table 3 is the apparent activation energy).

$$\ln(\frac{\beta}{T_p^2}) = -\frac{E_a}{RT_P} + \ln(\frac{AR}{E_a}) \tag{1}$$

$$E_o = -\frac{R}{1.052}\frac{d\ln\beta}{d(1/T_p)} \tag{2}$$

$$T_{p0} = T_p + a\beta + b\beta^2 + c\beta^3 \tag{3}$$

$$T_b = \frac{E_a - \sqrt{E_a - 4E_aRT_{p0}}}{2R} \tag{4}$$

where β is the heating rate (in K·min^{-1}), T_p is the temperature of the exothermic peak (in K), R is the ideal gas constant (8.314J·mol^{-1}·K^{-1}), E_a is the activation energy (in kJ·mol^{-1}), A is the preexponential factor (in s^{-1}), R^2 is the correlation coefficient, T_{p0} is the extrapolated peak temperature when $\beta \to 0$ and T_b is the critical temperature of thermal explosion.

Table 3. Thermal decomposition kinetic parameters of RDX, C/RDX physical mixture and C/RDX composite

Sample	β [K·min^{-1}]	T_p [K]	T_{p0} [K]	T_b [K]	E_a [kJ·mol^{-1}]		lgA [s^{-1}]	R^2	
					Kissinger	Ozawa	Kissinger	Kissinger	Ozawa
RDX	5	236.12	224.35	237.86	160.59	169.21	16.049	0.9987	0.9988
	10	245.61							
	15	250.34							
	20	254.38							
C/RDX physical mixture	5	209.13	185.69	199.51	134.45	142.62	14.096	0.9995	0.9995
	10	219.67							
	15	224.02							
	20	228.98							
C/RDX composite	5	193.09	180.87	197.17	112.85	120.78	12.148	0.9971	0.9975
	10	198.83							
	15	209.81							
	20	214.71							

It can be observed that the activation energy values obtained by the Kissinger and Ozawa methods are highly consistent, and the calculated results have good correlation. The apparent activation energy values for both the C/RDX physical mixture and the C/RDX composite decrease with the porous carbon present. In comparison to RDX, the apparent activation energy values for the C/RDX physical mixture and the C/RDX composite are decreased by 26.14, 26.59, and 47.74, 48.43 $kJ \cdot mol^{-1}$, the critical temperature of thermal explosion is decreased by 38.35 and 40.69 °C, and the T_{p0} is decreased by 38.65 and 43.47 °C, all respectively. The decomposition temperature of the C/RDX composite was significantly advanced, the decomposition rate and the depth of the decomposition reaction were also significantly improved, which caused the heat released to be increase and more concentrated. It would increase the burning rate of an RDX propellant.

3.6 Sensitivity

The impact, friction and electrostatic discharge sensitivities of RDX, the C/RDX physical mixture and the C/RDX composite were tested, as shown in Table 4. The impact sensitivity of pure RDX, C/RDX physical mixture and C/RDX composite were 8.72, 11.76 and 17.64 J, respectively, and the impact sensitivity of C/RDX physical mixture and C/RDX composite were 1.35- and 2.02-fold lower than that for pure RDX, respectively. Similarly, the friction sensitivity of pure RDX, C/RDX physical mixture and C/RDX composite were 146.28, 228.72 and 293.41 N, respectively. The friction sensitivity of the C/RDX physical mixture and the C/RDX composite were 1.56- and 2-fold lower than for pure RDX, respectively. The electrostatic discharge sensitivity of pure RDX, C/RDX physical mixture and C/RDX composite were 0.18, 0.26 and 0.38 J, respectively; and the electrostatic sensitivity of the C/RDX physical mixture and the C/RDX composite were 1.44- and 2.11-fold lower than that of pure RDX, respectively. Compared with other types of porous carbon composite energetic materials, the C/RDX composite had higher mechanical and electrostatic stability.

Table 4. Impact, friction and electrostatic discharge sensitivities of the RDX, C/RDX physical mixture and C/RDX composite

Material	Impact sensitivity [J]	Friction sensitivity [N]	Electrostatic discharge sensitivity [J]
RDX	8.82	146.28	0.18
C/RDX physical mixture	11.76	228.72	0.26
C/RDX composite	17.64	293.41	0.38

Compared with simple physical mixing, RDX filled porous carbon could reduce the friction between them, reducing the sensitivity to external stimuli and the chance of hotspots. Porous carbon, having high thermal conductivity and electrical conductivity, could effectively transfer heat and transport electrons, reducing the probability of hotspots and the accumulation of electrons in RDX.

4. Conclusions

- During this preparative process, acetone was selected as the solvent because of its low boiling point and high solubility for RDX, which also meant that a shorter time could be used for vacuum drying. In addition, a simple ultrasonic stirring process and vacuum drying were selected to realize the recrystallization operation, and finally the C/RDX nanocomposite energetic material was obtained. This C/RDX composite material stands out among other types of porous carbon composite energetic materials due to the easy availability of the raw materials, a simple process, low cost and high stability.
- In conclusion, through the ultrasonic stirring treatment, the micropores of the porous carbon frames enabled efficient impregnation by the RDX solution, followed by the formation of porous carbon/RDX nanocomposite energetic materials, and their physicochemical properties were characterized. The calculated results of kinetic and thermodynamic parameters indicated that C/RDX composite possessed high thermolysis activity; and the impact, friction and electrostatic sensitivity was greatly decreased. Overall, the porous carbon composite is a potentially practical composite that can be used as a nanostructured energetic material with high performance.

Supporting Information

See the supporting information for the sensitivity test methods of explosives (MIL-STD-1751A).

Acknowledgement

The authors acknowledge the support of the instrument and equipment fund of the Key Laboratory of Special Energy, Ministry of Education, Nanjing University of Science and Technology

Conflict of Interest

The authors declare no conflict of interest.

References

[1] Van der Heijden, A.E.D.M.; Bouma, R.H.B.; van der Steen, A.C.; Fischer, H.R. Application and Characterization of Nanomaterials in Energetic Compositions. *MRS Online Proc. Libr.* **2003**, *800*(1): 191-208; https://doi.org/10.1557/PROC-800-AA5.6.

[2] Puszynski, J. Processing and Characterization of Aluminum-based Nanothermites. *J. Therm. Anal. Calorim.* **2009**, *96*(3): 677-685; https://doi.org/10.1007/s10973-009-0037-0.

[3] Sreekumar, P.; Jin, O.Y.; Hoon, H.H. Nanoenergetic Composites with Fluoropolymers: Transition from Powders to Structures. *Molecules* **2022**, *27*(19): 6598-6598; https://doi.org/10.3390/MOLECULES27196598.

[4] DeVolder, M.F.L.; Tawfick, S.H.; Baughman, R.H.; Hart, A.J. Carbon Nanotubes: Present and Future Commercial Applications. *Science* **2013**, *339*(6119): 535-539; https://doi.org/10.1126/science.1222453.

[5] Ge, S.; Lan, F.; Yu, F.; Yu, J. Applications of Graphene and Related Nanomaterials in Analytical Chemistry. *New J. Chem*. **2015**, *39*(4): 2380-2395.

[6] Zhai, Y.; Zhu, Z.; Dong, S. Carbon-Based Nanostructures for Advanced Catalysis. *ChemCatChem* **2015**, *7*(18): 2806-2815; https://doi.org/10.1002/cctc.201500323.

[7] Zhang, M.; Zhao, F.; Yang, Y.; Li, H.; An, T.; Zhang, J. The Effect of rGO-Fe_2O_3 Nanocomposites with Spherical, Hollow and Fusiform Microstructures on the Thermal Decomposition of TKX-50. *J. Phys. Chem. Solids* **2021**, *153*: 109982; https://doi.org/10.1016/J.JPCS.2021.109982.

[8] Nguyen, T.D.; Nguyen, M.T.N.; Lee, J.S. Carbon-Based Materials and Their Applications in Sensing by Electrochemical Voltammetry. *Inorganics* **2023**, *11*(2): 81-81; https://doi.org/10.3390/INORGANICS11020081.

[9] Yuan, S.; Lai, Q.; Duan, X.; Wang, Q. Carbon-based Materials as Anode Materials for Lithium-Ion Batteries and Lithium-Ion Capacitors: A Review. *J. Energy Storage* **2023**, *61*: paper 106716; https://doi.org/10.1016/J.EST.2023.106716.

[10] Ren, X.; Zhao, S.; Han, Z.; Xing, X. Research Progress on Preparation Methods, Composite Systems, and Properties of Nanocomposite Energetic Materials. (in Chinese) *Materials Introduction* **2019**, *33*(23): 3939-3948.

[11] Wen, X.; Wang, J.; Zhang, N.; Huang, D.; Yu, H. Research Progress in the Application of Functionalized Carbon Nanomaterials in the Field of Energetic Materials. (in Chinese) *New Chem. Mater*. **2023**, *51*(02): 10-13; https://doi.org/10.19817/j.cnki.issn1006-3536.2023.02.003.

[12] Li, Z.M.; Zhou, M.R.; Zhang, T.L.; Zhang, J.G.; Yang, L.; Zhou, Z.N. The Facile Synthesis of Graphene Nanoplatelet-Lead Styphnate Composites and Their Depressed Electrostatic Hazards. *J. Mater. Chem. A* **2013**, *1*(41): 12710-12714; https://doi.org/10.1039/c3ta13177g.

[13] Yan, Q.-L.; Gozin, M.; Zhao, F.-Q.; Cohen, A.; Pang, S.-P. Highly Energetic Compositions Based on Functionalized Carbon Nanomaterials. *Nanoscale* **2016**, *8*(9): 4799-4851; https://doi.org/10.1039/C5NR07855E.

[14] Yu, J.; Wang, J.; Liu, Y.; Yu, Y.; Yuan, J.; Jin, S. Preparation and Properties of CL-20/Open Multi Walled Carbon Nanotube Composite Energetic Material. (in Chinese) *J. Explos. Mater.* **2017**, *40*(3): 72-76.
[15] Kent, R.V.; Vaid, T.P.; Boissonnault, J.A.; Matzger, A.J. Adsorption of Tetranitromethane in Zeolitic Imidazolate Frameworks Yields Energetic Materials. *Dalton Trans.* **2019**, *48*(22): 7509-7513; https://doi.org/10.1039/c9dt01254k.
[16] Pichot, V.; Comet, M.; Miesch, J.; Spitzer, D. Nanodiamond for Tuning the Properties of Energetic Composites. *J. Hazard. Mater*. **2015**, *300*: 194-201; https://doi.org/10.1016/j.jhazmat.2015.06.039.
[17] Guillevic, M.; Pichot, V.; Fioux, P.; Schnell, F.; Spitzer, D. Nanodiamond-based Energetic Core-Shell Composites: The Route Towards Safer Materials. *Diamond Relat. Mater.* **2019**, *93*: 150-158; https://doi.org/10.1016/j.diamond.2019.02.006.
[18] Li, H.; Ren, H.; Jiao, Q.; Du, S.; Yu, L. Fabrication and Properties of Insensitive CNT/HMX Energetic Nanocomposites as Ignition Ingredients. *Propellants Explos. Pyrotech.* **2016**, *41*(1): 126-135; https://doi.org/10.1002/prep.201500029.
[19] Zhang, X.; Hao, L. Preparation and Catalytic Activity of M_2O_3/CNTs (M = Y, Nd, Sm) Nanocomposites by Solvothermal Process. *J. Nanomater.* **2018**, *2018*: 1-8; https://doi.org/10.1155/2018/3635164.
[20] Wei, H.; Liu, X.-w.; Hu, Y.; Tang, H.-l.; Ye, Y.-h.; Shen, R.-q. Preparation and Characterization of Silicon-based $Cu(N_3)_2$@CNTs Composite Energetic Film. (in Chinese) *Chin. J. Energ. Mater.* **2020**, *28*(06): 557-563; https://doi.org/10.11943/CJEM2019166.
[21] Zhang, C.; Cao, X.; Xiang, B. Sandwich Complex of TATB/Graphene: An Approach to Molecular Monolayers of Explosives. *J. Phys. Chem. C* **2010**, *114*(51): 22684-22687.
[22] McCrary, P.D.; Beasley, P.A.; Alaniz, S.A.; Griggs, C.S.; Frazier, R.M.; Rogers, R.D. Graphene and Graphene Oxide Can "Lubricate" Ionic Liquids Based on Specific Surface Interactions Leading to Improved Low-Temperature Hypergolic Performance. *Angew. Chem., Int. Ed.* **2012**, *51*(39): 9784-9787; https://doi.org/10.1002/anie.201205126.
[23] Wang, H.; Cao, X.; Wu, J.; Xu, Y.; Shang, Y. Preparation and Thermal Decomposition Characteristics of TKX-50/GO Composite Energetic Materials. (in Chinese) *J. Explos.* **2020**, *43*(6): 631-635; https://doi.org/10.14077/j.issn.1007-7812.201908021.
[24] Song, Y.; Huang, Q.; Zhang, J.; Zhang, Y.; Jin, B.; Peng, R. Interaction-Enhanced Coating of Energetic Material: A Generally Applicable Method for the Desensitization. *Propellants Explos. Pyrotech.* **2022**, *47*(9): 202100256; https://doi.org/https://doi.org/10.1002/prep.202100256.
[25] Liu, R.; Zhao, W.; Zhang, T.; Yang, L.; Zhou, Z.; Zhang, J. Particle Refinement and Graphene Doping Effects on Thermal Properties of Potassium Picrate. *J. Therm. Anal. Calorim.* **2014**, *118*(1): 561-569; https://doi.org/10.1007/s10973-014-3980-3.
[26] Li, Z.; Wang, Y.; Zhang, Y.; Liu, L.; Zhang, S. CL-20 Hosted in Graphene Foam as a High Energy Material with Low Sensitivity. *RSC Adv.* **2015**, *5*(120): 98925-98928.

[27] Liu, T.; Geng, C.; Zheng, B.; Li, S.; Luo, G. Encapsulation of Cyclotetramethylene-tetranitramine (HMX) by Electrostatically Self-assembled Graphene Oxide for Desensitization. *Propellants Explos. Pyrotech.* **2017**, *42*(9): 1057-1065; https://doi.org/10.1002/prep.201700053.
[28] Su, Y.; Sun, Y.; Zhao, J. Interaction Mechanisms of Insensitive Explosive FOX-7 and Graphene Oxides from Ab Initio Calculations. *Nanomater.* **2019**, *9*(9): 1290; https://doi.org/10.3390/nano9091290.
[29] Zhang, T.; Guo, Y.; Li, J.; Guan, Y.; Guo, Z.; Ma, H. High Catalytic Activity of Nitrogen-Doped Graphene on the Thermal Decomposition of CL-20. *Propellants Explos. Pyrotech.* **2018**, *43*(12): 1263-1269; https://doi.org/10.1002/prep.201800014.
[30] Yu, J.; Wang, J.; Liu, Y.; Yu, Y.; Yuan, J. Preparation and Properties of CL-20/GO Nanocomposite Energetic Materials. (in Chinese) *Sci. Technol. Eng.* **2017**, *17*(12): 93-96.
[31] Van Riet, R.; Amayuelas, E.; Lodewyckx, P.; Lefebvre, M.H.; Ania, C.O. Novel Opportunities for Nanoporous Carbons as Energetic Materials. *Carbon* **2020**, *164*(C): 129-132; https://doi.org/10.1016/j.carbon.2020.03.061.
[32] Shin, M.K.; Kim, M.H.; Kim, G.Y.; Kang, B.; Chae. J.S.; Haam, S. Highly Energetic Materials-Hosted 3D Inverse Opal-like Porous Carbon: Stabilization/Desensitization of Explosives. *ACS Appl. Mater. Interfaces* **2018**, *10*(50): 43857-43864; https://doi.org/10.1021/acsami.8b11591.
[33] Qi, W.; Wang, M. Size and Shape Dependent Melting Temperature of Metallic Nanoparticles. *Mater. Chem. Phys.* **2004**, *88*(2): 280-284; https://doi.org/10.1016/j.matchemphys.2004.04.026.
[34] Huang, H.; Shi, Y.; Yang, J. Thermal Characterization of the Promising Energetic Material TKX-50. *J. Therm. Anal. Calorim.* **2015**, *121*(2): 705-709; https://doi.org/10.1007/s10973-015-4472-9.

Received: April 22, 2023
Revised: September 26, 2023
First published online: September 28, 2023